Available online at www.sciencedirect.com
ScienceDirect
Biomaterials 29 (2008) 1329–1344
Biomaterials
www.elsevier.com/locate/biomaterials

The development of binary Mg–Ca alloys for use as biodegradable materials within bone

Zijian Li [a,b], Xunan Gu [a], Siquan Lou [b], Yufeng Zheng [a,*]

[a] *LTCS, College of Engineering, Peking University, Beijing 100871, China*
[b] *Department of Orthopedics, Peking University Third Hospital, Beijing 100083, China*

Received 1 November 2007; accepted 16 December 2007
Available online 11 January 2008

Abstract

Binary Mg–Ca alloys with various Ca contents were fabricated under different working conditions. X-ray diffraction (XRD) analysis and optical microscopy observations showed that Mg–xCa ($x = 1–3$ wt%) alloys were composed of two phases, α(Mg) and Mg_2Ca. The results of tensile tests and *in vitro* corrosion tests indicated that the mechanical properties could be adjusted by controlling the Ca content and processing treatment. The yield strength (YS), ultimate tensile strength (UTS) and elongation decreased with increasing Ca content. The UTS and elongation of as-cast Mg–1Ca alloy (71.38 ± 3.01 MPa and 1.87 ± 0.14%) were largely improved after hot rolling (166.7 ± 3.01 MPa and 3 ± 0.78%) and hot extrusion (239.63 ± 7.21 MPa and 10.63 ± 0.64%). The *in vitro* corrosion test in simulated body fluid (SBF) indicated that the microstructure and working history of Mg–xCa alloys strongly affected their corrosion behaviors. An increasing content of Mg_2Ca phase led to a higher corrosion rate whereas hot rolling and hot extrusion could reduce it. The cytotoxicity evaluation using L-929 cells revealed that Mg–1Ca alloy did not induce toxicity to cells, and the viability of cells for Mg–1Ca alloy extraction medium was better than that of control. Moreover, Mg–1Ca alloy pins, with commercial pure Ti pins as control, were implanted into the left and right rabbit femoral shafts, respectively, and observed for 1, 2 and 3 months. High activity of osteoblast and osteocytes were observed around the Mg–1Ca alloy pins as shown by hematoxylin and eosin stained tissue sections. Radiographic examination revealed that the Mg–1Ca alloy pins gradually degraded *in vivo* within 90 days and the newly formed bone was clearly seen at month 3. Both the *in vitro* and *in vivo* corrosion suggested that a mixture of $Mg(OH)_2$ and hydroxyapatite formed on the surface of Mg–1Ca alloy with the extension of immersion/implantation time. In addition, no significant difference ($p > 0.05$) of serum magnesium was detected at different degradation stages. All these results revealed that Mg–1Ca alloy had the acceptable biocompatibility as a new kind of biodegradable implant material. Based on the above results, a solid alloy/liquid solution interface model was also proposed to interpret the biocorrosion process and the associated hydroxyapatite mineralization.

Keywords: Mg–Ca alloy; Biocorrosion; Biocompatibility; Implant materials; Hydroxyapatite

1. Introduction

Magnesium alloys would dissolve readily in aqueous solution especially that contains chloride ion [1,2]. This unique and intriguing characteristic recently has inspired the biomaterial researchers to develop them as a new kind of biodegradable material [3–9].

To our knowledge, the previous studies on biomedical magnesium alloys mainly focused on the Mg–Al and Mg–RE alloy systems [4–8]:

(1) *Mg–Al alloy system*. Witte et al. [4] had reported that the implantation of AZ31 and AZ91 alloy sample rods, compared to the polymer, increased the newly formed bone, and the corrosion layer of both alloys displayed an

* Corresponding author. Department of Advanced Materials and Nanotechnology, College of Engineering, Peking University, Beijing 100871, PR China. Tel./fax: +86 10 6276 7411.
E-mail address: yfzheng@pku.edu.cn (Y. Zheng).

0142-9612/$ - see front matter © 2007 Elsevier Ltd. All rights reserved.
doi:10.1016/j.biomaterials.2007.12.021

accumulation of biological calcium phosphates. Heublein et al. [6] had reported that the degradation of AE21 stent (4 mg) in coronary artery was considered to be linear and drew the conclusion that the vascular implants consisting of magnesium alloys seemed to be a realistic alternative to permanent implants.

(2) *Mg–RE alloy system*. The *in vivo* corrosion of LAE442 and WE43 were also investigated by Witte et al. [4] with the same procedure as that of AZ31 and AZ91. A much slow corrosion rate was recorded for LAE442, while AZ31, AZ91 and WE43 were found to degrade at similar rates. A Biotronik's Mg absorbable metal stent (AMS) (with 10 wt% of rare earth) had been successfully used in one preterm baby with an artificial pulmonary artery stenosis and the 4-month degradation process was clinically well tolerated, despite the small size of the baby [7]. However, another case of the implantation of AMS stent into a newborn with severely impaired heart function due to a long segment recoarctation after a complex surgical repair, was not well tolerated [8,10].

Clearly, to guarantee the biosafety of biodegradable materials, the constitutional elements of magnesium-based alloys should be toxic free. To address this point, the alloying elements aluminum and rare earth seem not to be the best adding elements. Aluminum is well known as a neurotoxicant and its accumulation has been suggested to be an associated phenomenon in various neurological disorders as dementia, senile dementia and Alzheimer disease [11]. Severe hepatotoxicity has been detected after the administration of cerium, praseodymium and yttrium [12].

In the present work, we select calcium as alloying element to develop binary magnesium–calcium alloys, with the following considerations. (1) It is well known that calcium is a major component in human bone and calcium is also essential in chemical signaling with cells [13]. (2) Ca has a low density (1.55 g/cm^3), which endues the Mg–Ca alloy system with the advantage of similar density to bone. (3) Magnesium is necessary for the calcium incorporation into the bone [14], which might be expected to be beneficial to the bone healing with the co-releasing of Mg and Ca ions.

According to the Mg–Ca binary phase diagram, the maximum solubility of Ca in Mg at 789.5 K is 1.34 wt% [15]. We design a range of Mg–Ca alloys, with the calcium content ranging from 1–20 wt%. Unfortunately the as-cast Mg–5, 10 and 20Ca alloys are found to be very brittle at room temperature and the plate samples can be easily broken by bare hands, so only the Mg–Ca alloys with low Ca contents (1–3 wt%) will be reported here.

In the present study, the feasibility of Mg–Ca alloys as biodegradable biomaterials for orthopedic applications will be evaluated according to the generalized requirements for biodegradable biomaterials [16,17], a comprehensive description on the actual *in vitro* and *in vivo* corrosion phenomenon of Mg–*x*Ca alloys will be done, and a reasonable biocorrosion model will be proposed.

2. Experimental procedure

2.1. Fabrication and sample preparation

Commercial pure Mg (99.9%) and Ca (99.9%) metal powders were melted and cast under a mixed gas atmosphere of SF_6 and CO_2 using a mild steel crucible. The as-cast ingots of Mg–*x*Ca alloys with different nominal calcium contents ($x = 1$, 2, 3 wt%) in quantities of 700–2000 g were obtained. The analyzed chemical compositions of the prepared alloys by energy dispersive spectrum (EDS) are given in Table 1. The Mg–1Ca alloy ingots were cut into 5 mm thick plates along the longitudinal direction, and then the plates were pre-heated to 400 °C for 1 h and hot rolled to about 2-mm thick sheets. The hot extruded Mg–1Ca alloy bars were obtained at a temperature of 210 °C with a reduction ratio of 17 by continuous extrusion of the ingot. Disk ($10 \times 10 \times 2$ mm^3) samples were prepared for the microstructure characterization, corrosion experiments and cytotoxicity tests, with the surface being polished up to 2000 grit. Pins (10 mm in length, 2.5 mm in diameter, a mimic to the AO company pin) were machined for animal implantation. All specimens were ultrasonically cleaned in acetone, absolute ethanol and distilled water and sterilized by ethylene oxide (ETO) at the sterilizing room of Peking University Third Hospital.

2.2. Microstructural characterization

X-ray diffractometer (Rigaku DMAX 2400) using CuK_α radiation was employed for the identification of the crystal structure of the phases. Optical microscope (Olympus BX51 M) was used to characterize the surface morphology, and the chemical composition was analyzed by EDS.

2.3. Tensile test

The tensile samples of as-cast Mg–*x*Ca alloys, as-rolled and as-extruded Mg–1Ca alloy were machined according to ASTM-E8-04 [18]. The tensile tests were carried out at a displacement rate of 1 mm/min by a SHIMADZU AG-100KNA materials testing machine.

2.4. Immersion test

The immersion test was carried out in the SBF [19] according to ASTM-G31-72 [20]. The pH was adjusted to 7.4, and the temperature was kept at 37 °C using water bath. After different immersion periods, the samples were removed from SBF, gently rinsed with distilled water, and dried at room

Table 1
Nominal and analyzed compositions of Mg–*x*Ca ($x = 1$–3 wt%) alloys

	Mg–1Ca		Mg–2Ca		Mg–3Ca	
	Mg	Ca	Mg	Ca	Mg	Ca
Nominal compositions/wt%	99	1	98	2	97	3
Analyzed compositions/wt%	99.03	1.06	97.98	2.02	96.79	3.21

temperature. Changes in the surface morphologies and the microstructures of the samples before and after immersion were characterized by environmental scanning electron microscopy (ESEM, AMRAY-1910FE), equipped with energy-disperse spectrometer (EDS) attachment, and XRD. The pH value of the SBF and the hydrogen evolution rate were monitored during the soaking experiment. An average of three measurements was taken for each group.

2.5. Electrochemical measurements

A three-electrode cell was used for electrochemical measurements. The counter electrode was made of platinum and the reference electrode was saturated calomel electrode (SCE). All potentials quoted were on the SCE scale. The exposed area of the working electrode (Mg−*x*Ca alloy plate samples) to the solution was 0.385 cm^2. All the measurements were carried out at a scan rate of 1 mV/s in a PAR Model 283 A potentiostat/galvanostat. The test milieu was SBF, and the test temperature was 37 °C.

2.6. Cytotoxicity test

L-929 cells were cultured in the Dulbecco's Modified Eagle's Medium (DMEM), 10% fetal bovine serum (FBS), 100 U/ml penicillin and 100 μg/ml streptomycin at 37 °C in a humidified atmosphere of 5% CO_2. The cytotoxicity tests were carried out by indirect contact. Extracts were prepared according to ISO 10993-5:1999 [21]. After 72 h incubation in a humidified atmosphere with 5% CO_2 at 37 °C, the extraction medium was serially diluted to 50% and 10% concentrations. The control groups involved the use of DMEM medium as negative controls and 0.64% phenol DMEM medium as positive controls. Cells were incubated in 96-well flat-bottomed cell culture plates at 5×10^3 cells/100 μl medium in each well and incubated for 24 h to allow attachment. The medium was then replaced with 100 μl of extracts. After incubating the cells in a humidified atmosphere with 5% CO_2 at 37 °C for 2, 4 and 7 days, 1 ml suspension was taken out and counted under an optical microscope. After that, 10 μl MTT was added to each well and the samples were incubated with MTT in DMEM. After the incubation at 37 °C for 4 h, 100 μl formazan solution was added into each well and 100 μl of the supernatant was measured spectrophotometrically at 570 nm by Elx-800 (BioTek instruments).

2.7. Animal implantation

2.7.1. Surgery

Eighteen adult male New Zealand rabbits of 2.5–3.0 kg in weight were used in this study, which were provided by the animal laboratory of Peking University Third Hospital. All rabbits were randomly assigned into three groups, in which four rabbits were implanted with one Mg−1Ca alloy pin into the left femoral shaft and one cortical bone c.p. Ti pin (AO company) into the right femoral shaft (named G1), the remaining two rabbits were implanted with two Mg−1Ca alloy pins into both femoral shafts (named G2). Animals were generally anesthetized for surgery and the femoral region was scrubbed with 25 g/L tincture of iodine and 70% ethanol. The pins were screwed into the rabbit's femoral shaft after pre-drilling with a 2 mm hand-operated drill. All animals received a subcutaneous injection of penicillin postoperation. Each group of rabbits was sacrificed 1, 2 and 3 months after surgery. Two milliliters of blood was collected from the helix vein of every rabbit to measure the change of serum magnesium before and 1, 2 and 3 months after the operation.

2.7.2. Histological and radiographic evaluations

Radiographs were performed to observe the healing process immediately after the surgery and before the removal of metallic pins. Bone samples around the pins and soft tissues around the pin cap were fixed in 10% formaldehyde solution. After the removal of pins, the bone samples were dehydrated and decalcified and the soft tissues were dehydrated. Tissues were embedded in paraffin and the histological evaluation was performed on hematoxylin and eosin stained sections.

2.7.3. Characterization of retrieved pins

The Mg−1Ca alloy pins were removed from femora and retrieved after drying in the air. The weight loss measurements were carried out, and the dimension, surface morphology and surface component of retrieved pins were characterized by ESEM, EDS and XRD techniques.

2.8. Statistical analysis

Statistical analysis was conducted to evaluate the difference in cell viability by the analysis of variance (ANOVA). Two-way *t*-test for paired data was used to compare the values of serum magnesium before and after the operation. The statistical significance was defined as 0.05.

3. Results

3.1. Microstructures and mechanical properties of Mg−Ca alloys

Fig. 1 showed the XRD patterns of as-cast Mg−*x*Ca alloys, as-rolled and as-extruded Mg−1Ca alloy samples. The formation of the second phase Mg_2Ca could be identified and the diffraction intensities that arose from Mg_2Ca phase increased with increasing Ca content. Fig. 2 showed the microstructures of as-cast Mg−*x*Ca alloys, as-rolled and as-extruded Mg−1Ca alloy, and the EDS results of as-cast Mg−3Ca alloy sample. The EDS analysis results indicated that the grain boundaries were rich in Ca (Fig. 2f), suggesting that the Mg_2Ca phase precipitated along the grain boundaries. The typical metallographic microstructure of α(Mg) primary grains with Mg_2Ca phase precipitating along the grain boundaries was seen in the case of Mg−2Ca and Mg−3Ca alloy samples (Fig. 2b, c). It could be seen that the grain size decreased after hot rolling and hot extrusion (Fig. 2d, e).

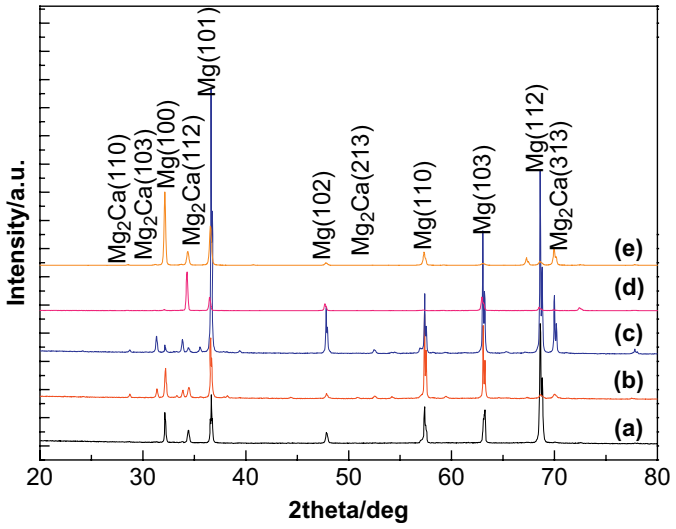

Fig. 1. X-ray diffraction patterns of (a) as-cast Mg−1Ca alloy, (b) as-cast Mg−2Ca alloy, (c) as-cast Mg−3Ca alloy, (d) as-rolled Mg−1Ca alloy, and (e) as-extruded Mg−1Ca alloy samples.

The mechanical properties of as-cast Mg−*x*Ca alloys, as-rolled and as-extruded Mg−1Ca alloy were shown in Fig. 3. It could be seen that the YS, UTS and elongation for as-cast Mg−*x*Ca alloy samples decreased with increasing Ca content. The YS, UTS and elongation increased largely after hot rolling and hot extrusion for as-cast Mg−1Ca alloy samples.

3.2. Immersion tests of Mg−Ca alloys

Fig. 4a−c showed the secondary electron images of the surface of Mg−*x*Ca ($x = 1-3$ wt%) alloy samples immersed in SBF for 5 h. As seen in Fig. 4a, Mg−1Ca alloy sample maintained the integrity of the corrosion film and the surface presented a crackled appearance due to the dehydration of the layer after drying in warm air and under the vacuum of the SEM chamber [22]. In the case of Mg−2Ca alloy, besides the crackled surface, some positions exhibited the peeled-off surface feature (typically area A in Fig. 4b) whereas other positions (typically area B in Fig. 4b) were still covered with integrated surface film. Micro-pores were observed on the surface film at high magnification (the inset picture in Fig. 4b, which corresponded to the area B in Fig. 4b). EDS results (Fig. 4d) showed that area A in Fig. 4b was rich in carbon, oxygen, magnesium, phosphorus and chloride. In contrast, low chloride atom ratio was found in area B in Fig. 4b (Fig. 4e). For the sample with 3 wt% calcium content, local areas of sample surface were undermined and many deep pits were left on the surface (Fig. 4c).

Fig. 5a−d showed the secondary electron images of Mg−1Ca and Mg−2Ca alloy samples surfaces immersed in SBF for 250 h. To the naked eyes, the entire samples were found to be covered with white precipitates and the square configuration of sample was severely destroyed. It should be noted that Mg−3Ca alloy plate degraded too fast and disintegrated into fragments after 24 h exposure to the aggressive test solution, therefore was not reported here. At low magnification (Fig. 5a, b), both the corroded Mg−1Ca and Mg−2Ca alloy samples showed compact surface morphologies, with a layer of corrosion product coated. At high magnification, in contrast to the dense film on Mg−1Ca alloy sample (Fig. 5c), some regular micro-pores (Fig. 5d) were seen in the case of Mg−2Ca alloy sample. EDS analysis results (Fig. 5e) showed the presence of carbon, oxygen, magnesium, phosphorus and calcium on the surface of dry 250 h immersed Mg−1Ca alloy sample.

Fig. 6a, b illustrated the XRD patterns of Mg−1Ca and Mg−2Ca alloy samples after immersing in SBF for different immersion periods. XRD spectra showed that $Mg(OH)_2$ was the dominant crystalline corrosion product in both alloy samples and the $Mg(OH)_2$ peak intensities increased with the extension of immersion period. Moreover, the special diffraction peaks (insets in Fig. 6a, b) in the 2theta range 20−35° indicated the formation of hydroxyapatite.

Fig. 7 showed the variation of the pH value of immersion solution as a function of immersion time. It could be seen that pH value raised from 7.4 at 0 h to the maximum of about 10.5 at 24 h, after which it fluctuated gradually, and stabilized finally at around 9.8 for both as-cast Mg−1Ca and Mg−2Ca alloy samples. In addition, the pH value increased much slowly during the immersion period for as-rolled and as-extruded Mg−1Ca alloy samples.

The hydrogen evolution during immersion was monitored and the results showed that the average hydrogen evolution rate from as-extruded Mg−1Ca alloy (0.040 ml/cm^2/h) was much less than that from as-cast Mg−1Ca alloy (0.136 ml/cm^2/h), as shown in Fig. 8.

3.3. Electrochemical measurements of Mg−Ca alloys

The electrochemical polarization curves of Mg−*x*Ca alloys ($x = 1-3$ wt%) in the SBF were shown in Fig. 9. Generally, the cathodic polarization curves were assumed to represent the cathodic hydrogen evolution through water reduction, while the anodic polarization curves represented the dissolution of magnesium [23]. It could be seen that the cathodic polarization current of hydrogen evolution reaction on Mg−3Ca alloy sample was much higher than that on Mg−1Ca alloy and Mg−2Ca alloy samples, which indicated that the over potential of the cathodic hydrogen evolution reaction was lower for Mg−3Ca alloy sample. As a result, the cathodic reaction was kinetically easier on the Mg−3Ca alloy sample than on the other two alloy samples.

Obviously the current plateaus with different breakdown potentials could be observed in the anodic parts of the curves in Fig. 9, which indicated the existence of some protective film on the surface of the Mg−*x*Ca alloy samples. The potential range of the current plateau for Mg−1Ca alloy sample (about 320 mV) was higher than those of Mg−2Ca alloy sample (210 mV) and Mg−3Ca alloy sample (170 mV), which indicated that the films on the Mg−1Ca alloy sample were much more protective than those on the Mg−2Ca alloy and Mg−3Ca alloy samples. Higher breakdown potentials were

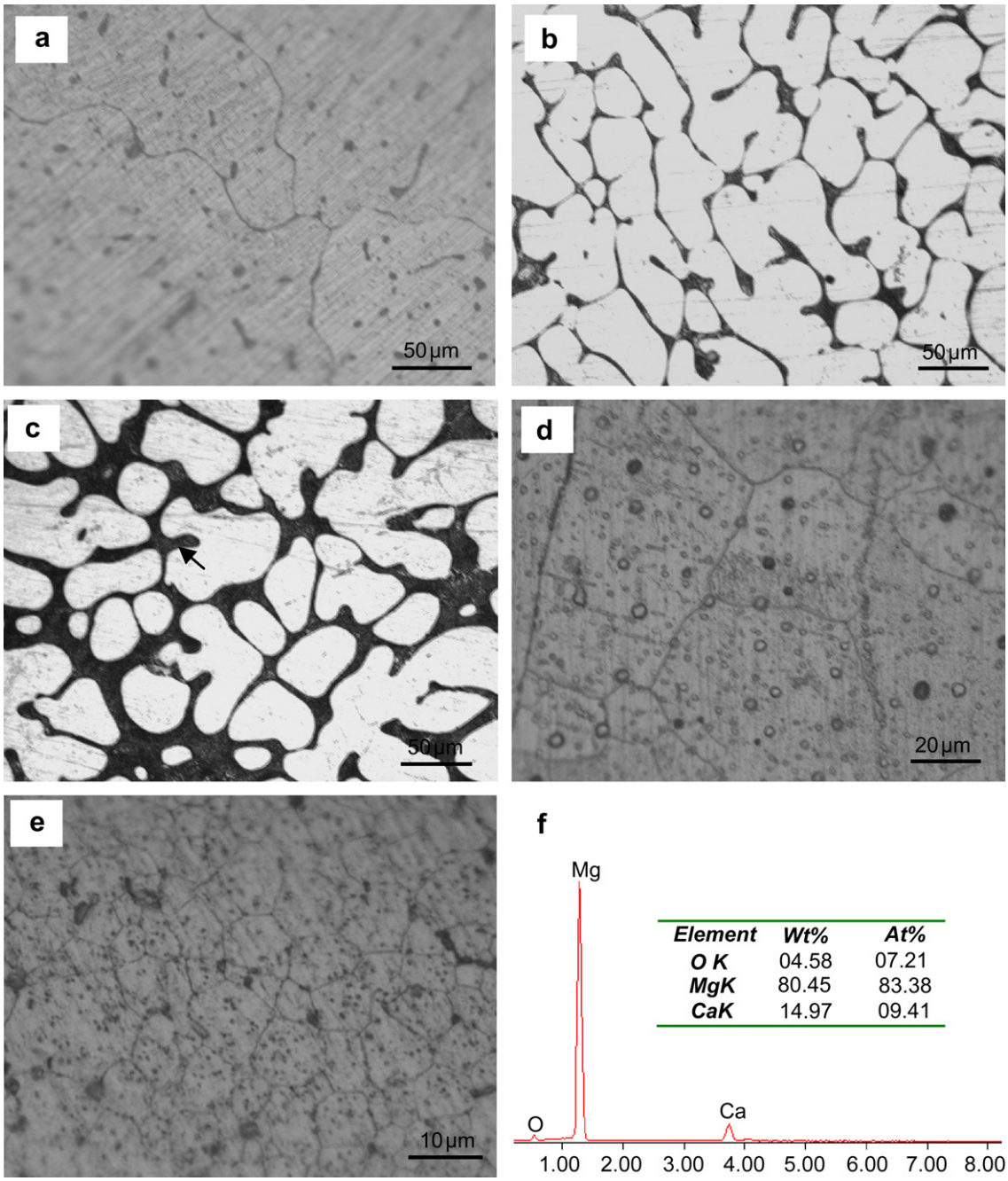

Fig. 2. Optical micrographs of (a) as-cast Mg−1Ca alloy, (b) as-cast Mg−2Ca alloy, (c) as-cast Mg−3Ca alloy, (d) as-rolled Mg−1Ca alloy, (e) as-extruded Mg−1Ca alloy samples, and (f) EDS spectrum corresponding to the area marked by an arrow in (c).

observed for as-rolled and as-extruded Mg−1Ca alloy samples, which indicated that the surface films on them were more protective than that on the as-cast Mg−*x*Ca alloy samples.

Fig. 10 showed the ESEM micrographs of sample surface after polarization experiments. The surface film of Mg−1Ca alloy sample was relatively flat and compact with less micro-cracks, suggesting that the Mg−1Ca alloy was more protective from the penetration of the electrolyte than the other two alloys and its surface film might reduce the corrosion rate effectively. According to ASTM-G102-89 [24], the corrosion rates derived from the corrosion current densities for as-cast Mg−1Ca, as-cast Mg−2Ca, as-cast Mg−3Ca alloy, as-rolled and as-extruded Mg−1Ca alloy samples were calculated to be 12.56, 12.98, 25.00, 1.63 and 1.74 mm/yr, respectively.

3.4. Cytotoxicity test of Mg−1Ca alloy

Mg−1Ca alloy was selected to further evaluate the cytotoxicity through examining both the viability and morphology of L-929 cells. Fig. 11 showed the cell viability cultured in 100%, 50% and 10% Mg−1Ca alloy extraction medium for 2, 4 and 7 days. It could be seen that cells cultured in Mg−1Ca alloy extracts showed a significant higher absorbance

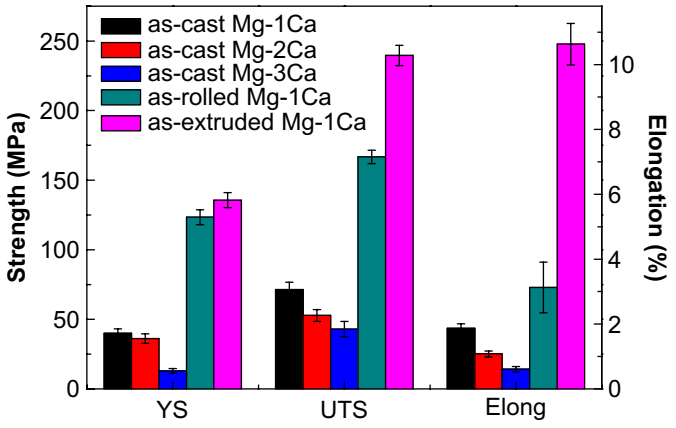

Fig. 3. Tensile properties of as-cast Mg−1Ca alloy, as-cast Mg−2Ca alloy, as-cast Mg−3Ca alloy, as-rolled Mg−1Ca alloy and as-extruded Mg−1Ca alloy samples at room temperature.

than the control. In addition, the cell viability was positively influenced by the higher extract concentration.

Fig. 12 showed the morphologies of L-929 cells cultured in the extraction media for a period of 2, 4 and 7 days. All the results for 100%, 50%, and 10% Mg−1Ca alloy extraction media and the controls exhibited a healthy morphology of cells with flattened spindle shape.

3.5. Animal tests of Mg−1Ca alloy

3.5.1. Serum magnesium measurements

Fig. 13 showed the changes of the serum magnesium levels in rabbits with one (G1) or two (G2) Mg−1Ca alloy pins for 1, 2 and 3 months implantation time. In the case of G1, the serum magnesium results showed no statistically significant difference ($p > 0.05$) between the preoperation and 1, 2 and 3 months postoperation. In the case of G2, a significant difference ($p < 0.05$) was found at 2 months postoperation.

3.5.2. Radiographic evaluation

Fig. 14 showed the radiographs of rabbit femora with implantation of Mg−1Ca alloy pin and c.p. Ti pin at 1, 2 and 3 months. The contrast of c.p. Ti pin (with higher density) was higher than that of the compact bone, and the profiles of c.p. Ti pins were distinct (Fig. 14a, b). For Mg−1Ca alloy pin, although a lower radiopacity was observed at the same X-ray dosage, its profile was still clear (Fig. 14c) immediately after the operation. Fig. 14 indicated Mg−1Ca alloy pins had degraded gradually during the whole experiment period, which was evident by the reducing diameter of pins. At month 3, the main structure of Mg−1Ca alloy pin was totally absorbed and an irregularly shaped hole was left in the implant position, which is indicated by a black triangle in Fig. 14h. Moreover, the periosteal reaction was observed around the Mg−1Ca alloy pin indicating the formation of new bone. The X-ray image at month 3 showed the circumferential osteogenesis (black triangle in Fig. 14h). However, no remarkable radiographic signs, indicating the new bone formation, were discovered around c.p. Ti pins during the experimental period (Fig. 14b). Gas shadows (arrow in Fig. 14d) were observed in soft tissues and bone marrow cavity around the Mg−1Ca alloy pins at month 1. Two months postoperation, the gas shadows vanished (Fig. 14f) without a special treatment. No adverse effects due to the gas formation were detected.

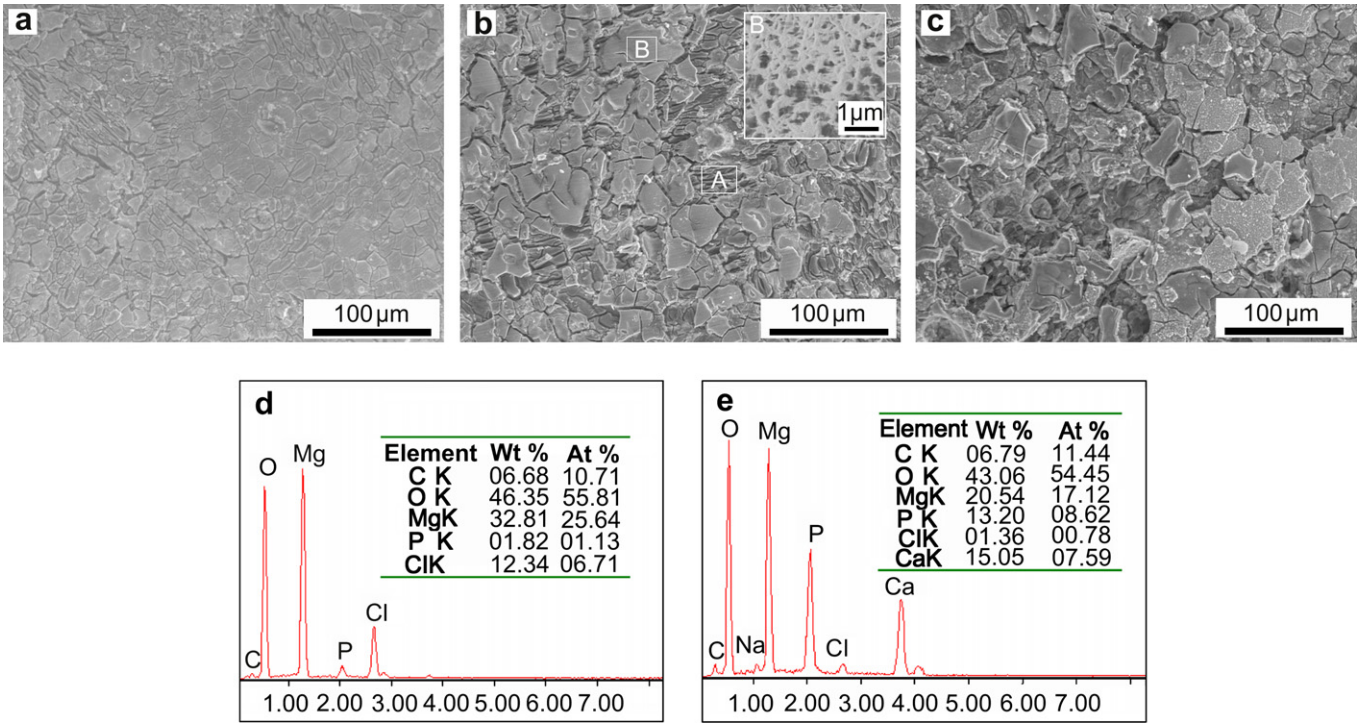

Fig. 4. SEM micrographs of (a) as-cast Mg−1Ca alloy, (b) as-cast Mg−2Ca alloy, (c) as-cast Mg−3Ca alloy after immersion in SBF for 5 h, (d) EDS spectrum of area A in (b), and (e) EDS spectra of area B in (b). Inset in (b) shows the magnified SEM image of area B (arrow−holes in the surface).

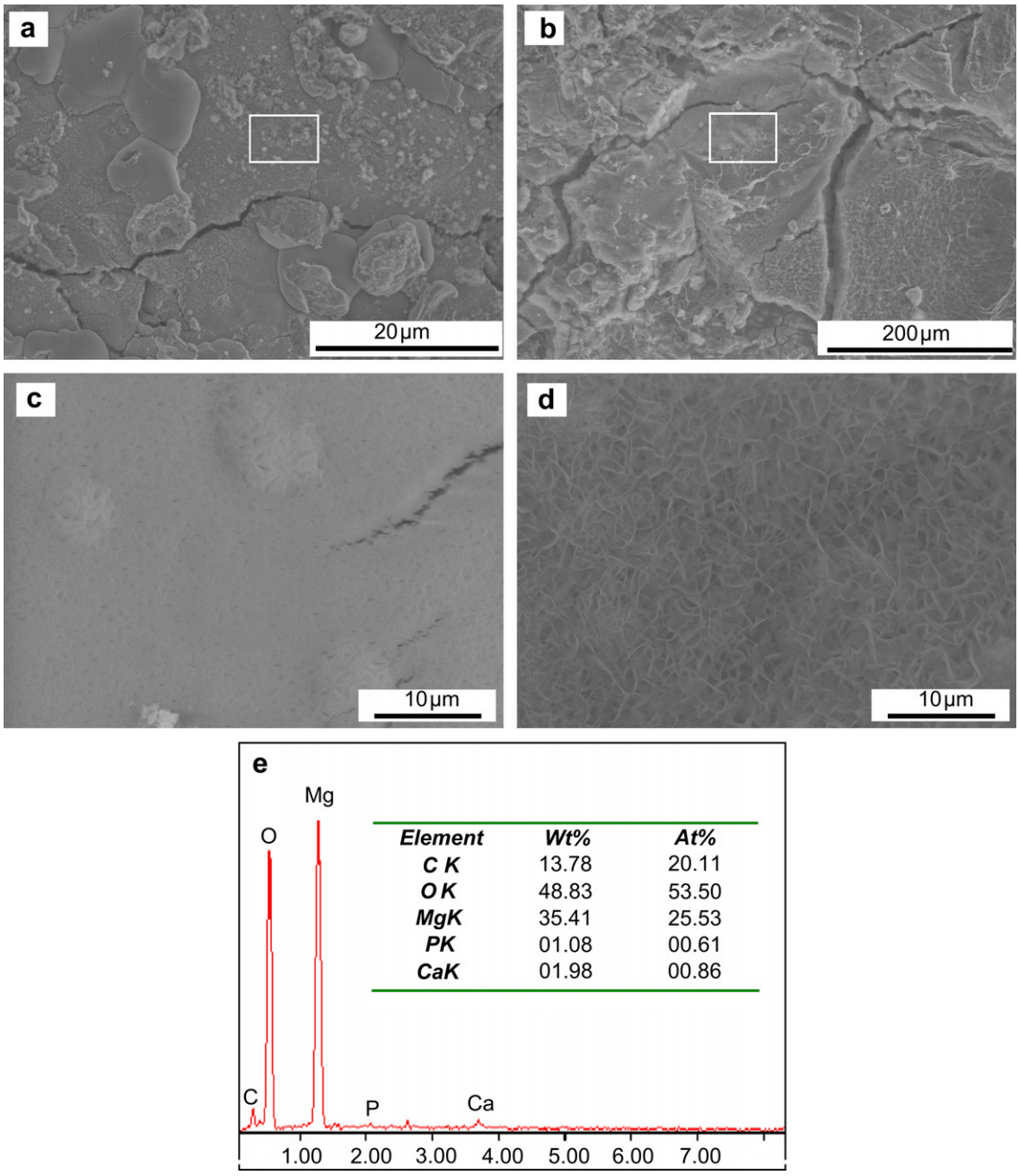

Fig. 5. SEM micrographs of (a) as-cast Mg−1Ca alloy, (b) as-cast Mg−2Ca alloy after immersion in SBF for 250 h, (c) high magnification image of the framed area in (a), (d) high magnification image of the framed area in (b), and (e) EDS spectrum of the framed area in (a).

3.5.3. Histological evaluation

Fig. 15 showed the tissue response to the c.p. Ti and Mg−1Ca alloy pins implantation at 1, 2 and 3 months. In the case of the control, the arrangement of bone trabecula was in good order and no evidence of newly formed bone was seen in the 3-month implantation time (Fig. 15a, b). In contrast, an active bone formation, which was evident by large number of osteoblasts (arrows in Fig. 15d, f, h) and the osteocytes (asterisks in Fig. 15d, f, h), were seen in the Mg−1Ca alloy group. At month 2, the formation of new bone was clearly seen, but the alignment of the osteocytes was disorganized. At month 3, the osteocytes were aligned in rows. Furthermore, some lymphocytes (circles in Fig. 15f) were identified at month 2 postoperation, but there was no visible evidence of multinucleated giant cells.

3.5.4. Characterization of the retrieved pins

Fig. 16 illustrated the macroscopic observation of the exposed femora with Mg−1Ca alloy pins implanted at 1, 2 and 3 months. It could be seen that a lot of white corrosion products were covered on the surface of Mg−1Ca alloy pins and the volume of Mg−1Ca alloy pins gradually decreased with increasing implantation time. Three months postimplantation, the main body of Mg−1Ca pin was totally absorbed leaving an

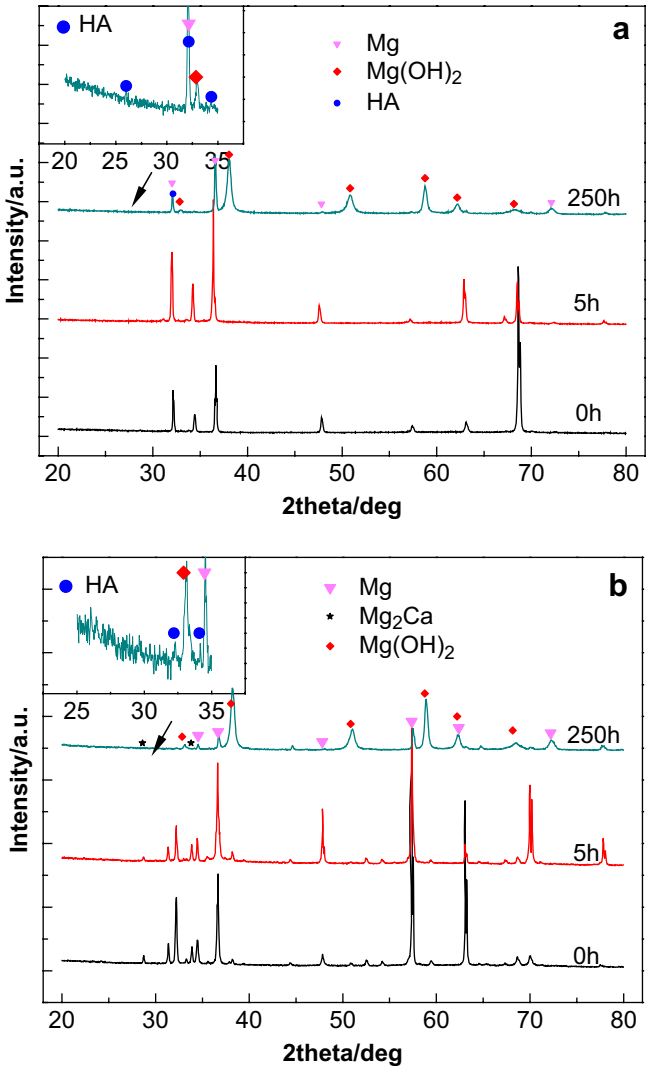

Fig. 6. X-ray diffraction patterns of (a) as-cast Mg–1Ca alloy, and (b) as-cast Mg–2Ca alloy immersed in SBF for 0, 5 and 250 h, respectively.

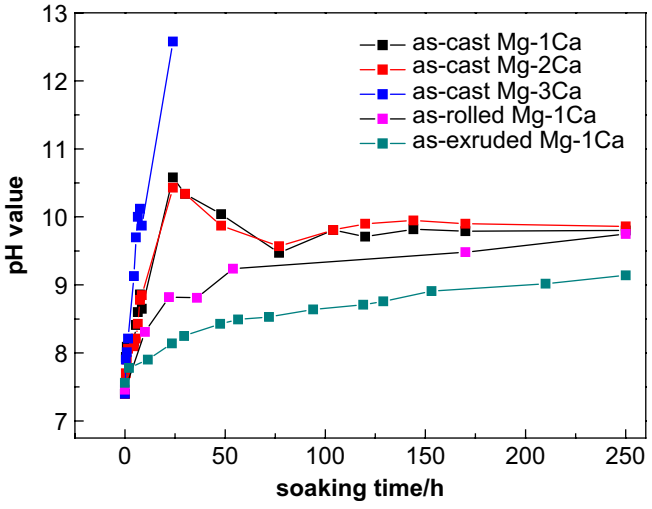

Fig. 7. The pH value of SBF incubating as-cast Mg–1Ca alloy, as-cast Mg–2Ca alloy, as-cast Mg–3Ca alloy, as-rolled Mg–1Ca alloy and as-extruded Mg–1Ca alloy samples as a function of immersion time.

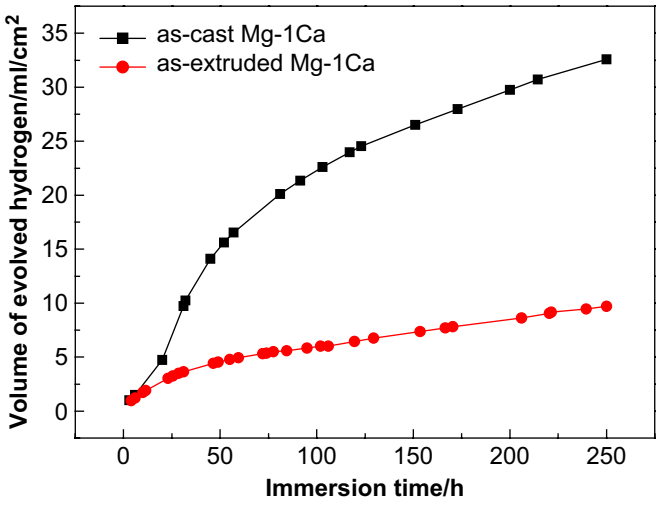

Fig. 8. The hydrogen evolution volumes of as-cast and as-extruded Mg–1Ca alloy samples as a function of the immersion time in SBF.

irregular shaped hole at the implant position (arrow in Fig. 16c).

Fig. 17a showed the images of the retrieved Mg–1Ca alloy pin at 1 month postoperation, indicating that Mg–1Ca alloy pin maintained the screw shape and a layer of aggregated substances covered on the pin. X-ray diffraction pattern showed that the mineral phases containing in this precipitate layer were $Mg(OH)_2$ and hydroxyapatite (Fig. 18). The presence of $Mg(OH)_2$ and hydroxyapatite was also supported by the EDS analysis (Fig. 17b), which revealed the presence of carbon, nitrogen, oxygen, magnesium, phosphorus, sulfur and calcium elements.

Fig. 19 shows the weight change of Mg–1Ca alloy pins after taking out from the femora as a function of the implantation time. It could be seen that the mass decreased throughout the implantation time, indicating a continuing biocorrosion process inside the rabbit femora. The average biocorrosion

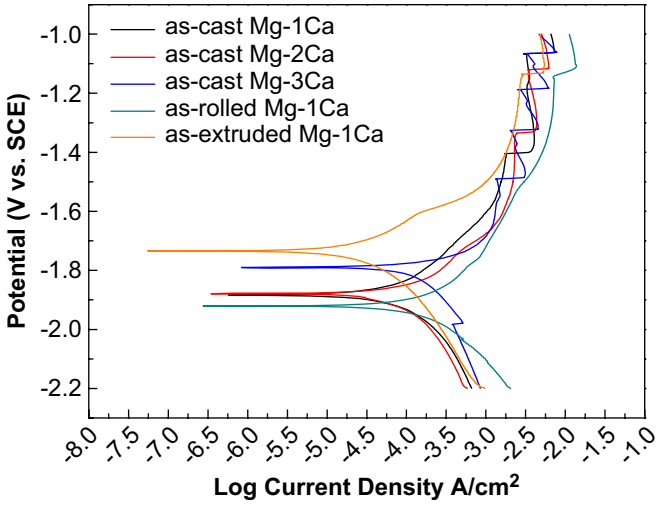

Fig. 9. Potentiodynamic polarization curves of as-cast Mg–1Ca alloy, as-cast Mg–2Ca alloy, as-cast Mg–3Ca alloy, as-rolled Mg–1Ca alloy and as-extruded Mg–1Ca alloy samples in SBF.

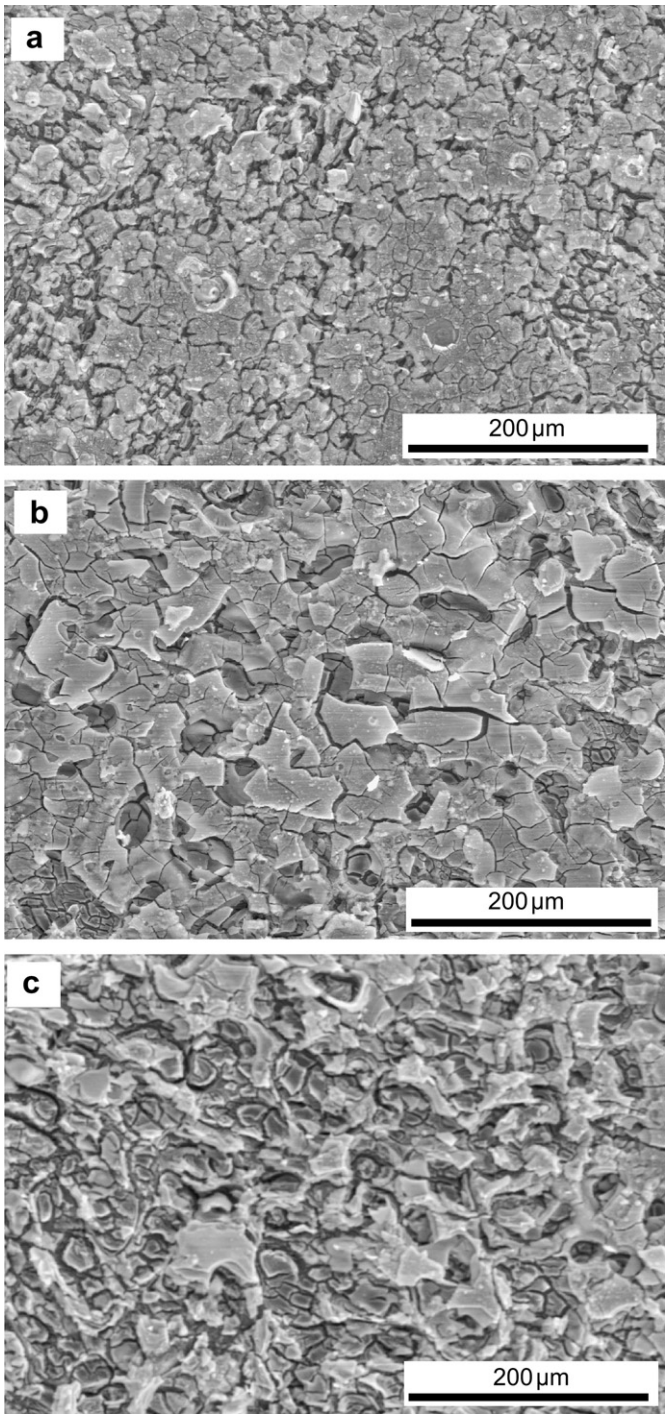

Fig. 10. SEM micrographs of (a) as-cast Mg−1Ca alloy, (b) as-cast Mg−2Ca alloy, and (c) as-cast Mg−3Ca alloy samples after polarization in SBF.

rate of Mg−1Ca alloy pins was calculated to be about 2.28 ± 0.13 mg/mm^2/yr in the present study.

4. Discussion

4.1. Mechanical properties and processibilities

It could be seen from Table 2 that the mechanical properties of hot rolled and hot extruded Mg−1Ca alloy samples were at

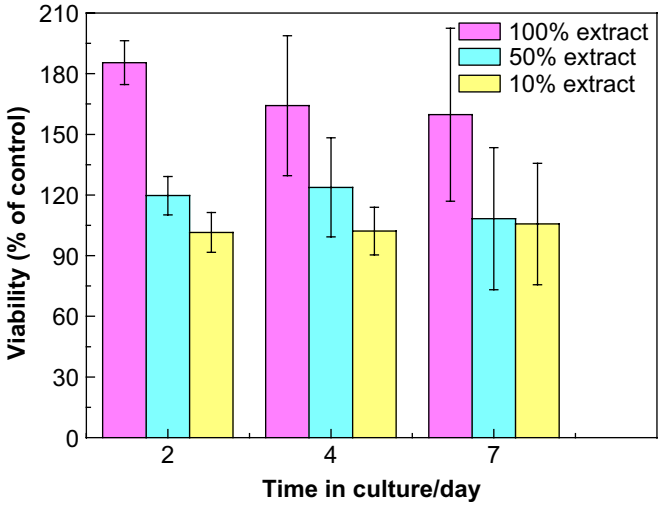

Fig. 11. L-929 cell viability expressed as a percentage of the viability of cells in the control after 2, 4 and 7 days of culture in Mg−1Ca alloy extraction media with 100%, 50%, and 10% concentrations, respectively.

the same level as that of the previously reported magnesium alloys for biomedical applications [25,26], and were higher than that of the degradable polymeric implant materials currently in use, such as u-HA/PLLA 50/50 with a tensile strength of 103 MPa [27]. Furthermore, Takeshi et al. [28] had found that the UTS of rapid solidified Mg−Ca alloy (2 wt%) was 380 MPa and the elongation was 7.3%. These implied that it would be possible to adjust the mechanical properties of Mg−*x*Ca alloy by mesne process to the acceptable values (200−400 MPa) for biomedical applications.

One of the advantages of magnesium alloys, compared to biodegradable polymers and ceramics, was ease of hot working, such as rolling, forging and extrusion [17]. Our present work on the machining, hot rolling, hot extrusion of Mg−1Ca alloy ingot and the work of Takeshi et al. [28] on the rapid solidification of Mg−2Ca alloy ingot, demonstrated the good processibility of Mg−Ca alloys.

4.2. In vitro and in vivo biocompatibility

The present *in vitro* test results demonstrated that the L-929 cells exhibited better growth in Mg−1Ca alloy extraction medium than in the control. The abundant magnesium ions released into the culture medium by the corrosion of Mg−1Ca alloy might contribute to the increased cell viability since they were found to simulate the integrin-mediated osteoblast response by facilitating the interaction of integrins with their cognate ligands [29,30]. The increased cell viability on Mg−1Ca alloy plate was somewhat in accordance with the recent study showing an enhanced marrow cell growth on pure Mg [3]. Zreiqat et al. [29] reported that magnesium ions modified bioceramic substrata could enhance the adhesion of human bone-derived cell (HBDC), and the HBDCs grown on the Mg^{2+}-modified bioceramic substrata were found to express significantly enhanced levels of $\alpha 5\beta 1$- and $\beta 1$-integrin receptors, which mediated the cell adhesion to biomaterial surfaces.

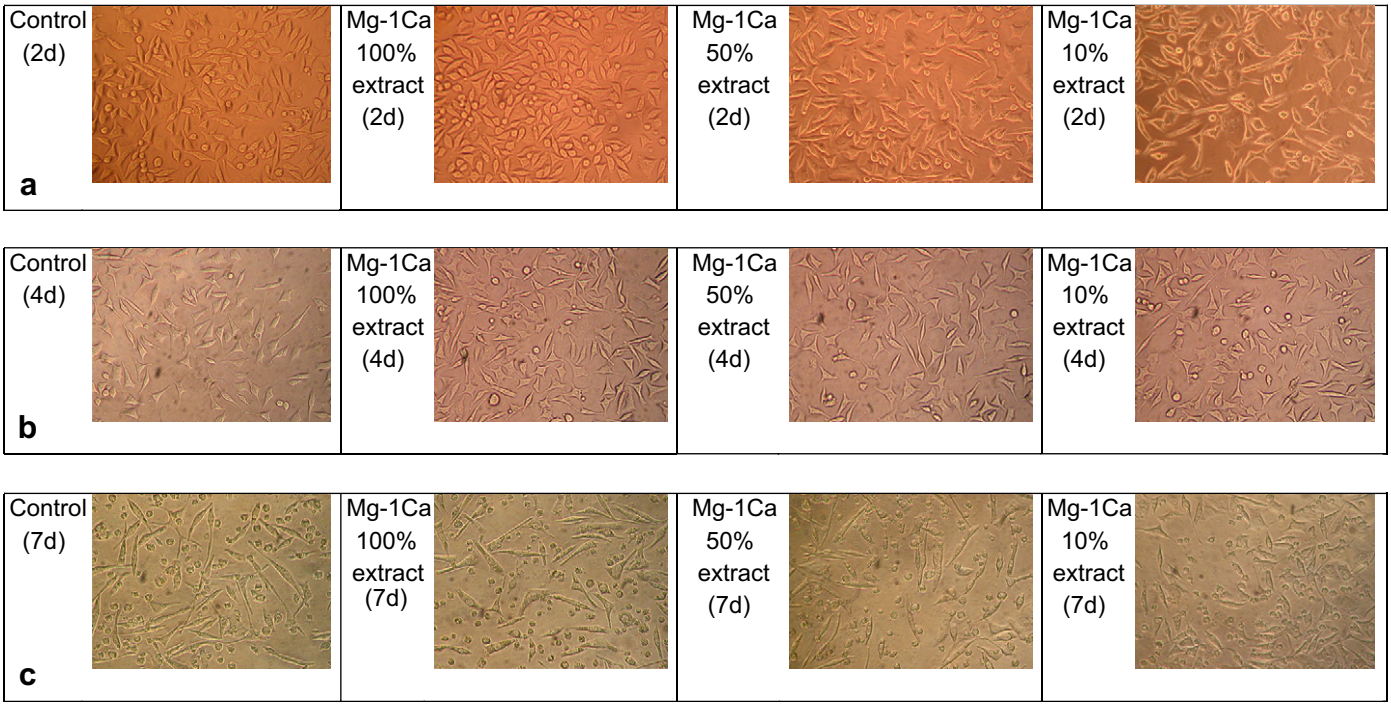

Fig. 12. Optical morphologies of L-929 cells that were cultured in the control and 100%, 50%, and 10% concentration Mg–1Ca alloy extraction medium for (a) 2 days, (b) 4 days and (c) 7 days.

Therefore, it might be assumed that the improvement of Mg–1Ca alloy in cell viability might arise from the facilitation in the early osteoblast response, and it could be inferred that the release of abundant Mg^{2+} might enhance the cell attachment and proliferation, which in turn resulted in the enhanced bone healing during *in vivo* animal tests. Moreover, the enhanced osteoblast adhesion, spreading, and growth on Ca-incorporated Ti surfaces had been revealed [31,32], which indicated that the release of Ca ions might also contribute to the increased viability on Mg–Ca alloy.

The present *in vivo* biocompatibility evaluation revealed the formation of a new bone around Mg–1Ca alloy pin 3 months postoperation in the rabbit femur, whereas no newly formed bone tissue was seen around the c.p. Ti pin. The facilitation of bone formation at Mg–1Ca alloy pin might be associated with the release of magnesium ions during the degradation process. It had been suggested that the dominant distribution of body magnesium located in bone [29] and the supplementing magnesium resulted in a significant increase in bone density and bone strength [33,34]. Moreover, it was reported that the presence of magnesium on orthopedic implants could enhance the adhesion of osteoblastic cells and promote optimal osteogenesis [29]. Therefore, magnesium might play an important role in the growth of bone tissue. In this study, the release of relatively large amount of magnesium ions might have contributed to the enhanced activity of osteoblast in the tissues around Mg–1Ca alloy pin (Fig. 15c–f). The newly formed bone was characterized by high activity and good alignment of osteocytes around the Mg–1Ca alloy pins (Fig. 15g, h), suggesting that the newly formed mineral apposition must have been present. An enhanced mineral apposition rate in magnesium-implanted bone specimens [4], accompanied with the high activity of osteocyte, might explain the formation of new bone.

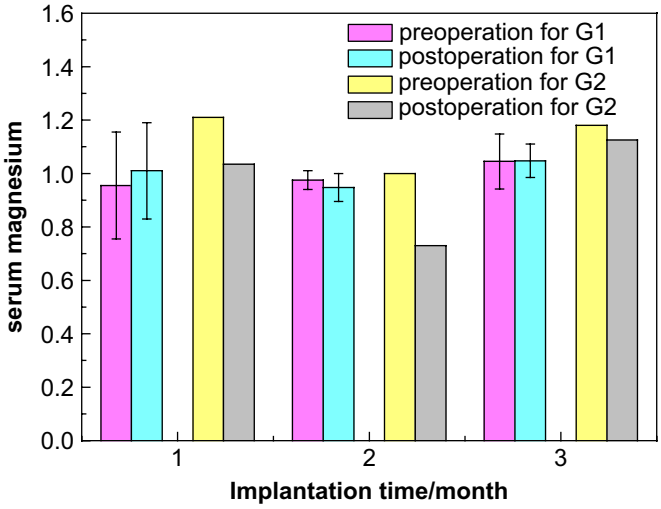

Fig. 13. Changes in serum magnesium levels of rabbits with one (G1) and two (G2) Mg–1Ca alloy pins after 1, 2 and 3 months implantation.

In the present work, no statistically significant differences in serum magnesium were found before operation and at 1, 2 and 3 months postoperation for G1. However, it was interesting to find that the serum magnesium of G2 decreased at 1, 2 and 3 months postoperation, compared to that of preoperation. This might be controlled by the self-regulation mechanism of organism and the surplus magnesium would be excreted from urine [33].

Hydrogen gas was another degradation product and was only detected in the early implantation time (Fig. 14d). This

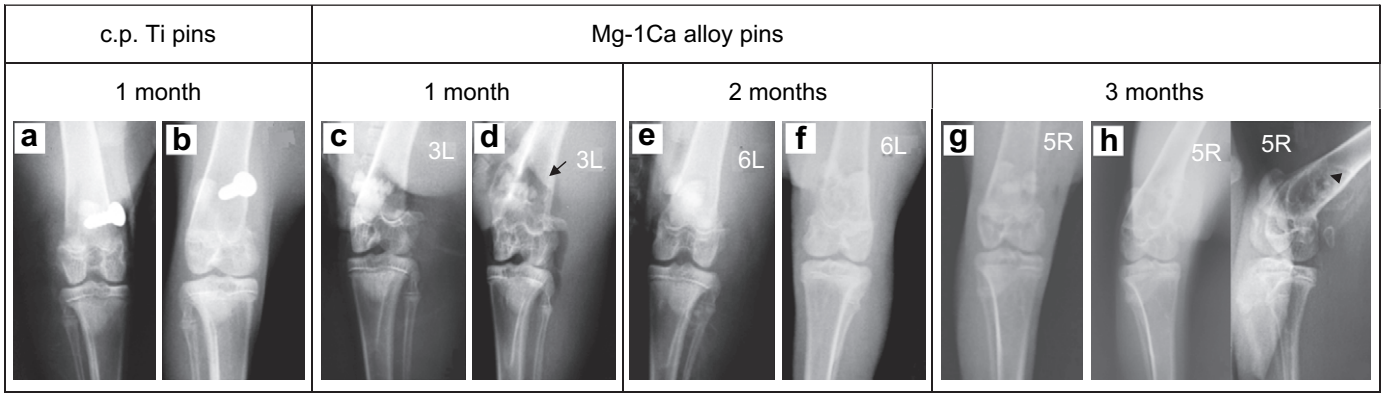

Fig. 14. Femora radiographs of rabbit with implants for different periods after surgery. (a and b) c.p. Ti pin at 1 month postoperation; (c and d) Mg–1Ca alloy pins at 1 month postoperation (the arrow marks the gas shadows); (e and f) Mg–1Ca alloy pins at 2 months postoperation; (g and h) Mg–1Ca alloy pins at 3 months postoperation (the black triangle marks the circumferential osteogenesis).

could be explained by the accelerated corrosion at the Mg–1Ca alloy pin surface due to the secondary acidosis resulting from the metabolic and resorptive processes after surgery [4]. Without any special treatment, hydrogen gas was found to be self-absorbed because the gas shadows were not observed at months 2 and 3. These results were consistent with the *in vivo* studies on other magnesium alloys, in which the hydrogen gas bubbles appeared at 1 week postoperation and disappeared later [4].

4.3. Biocorrosion and hydroxyapatite formation

A biocorrosion model at the alloy/aqueous solution interface was proposed to understand the corrosion processes and the subsequent hydroxyapatite formation, as shown in Fig. 20. The previous electrochemical mechanism of the pure magnesium [2] in aqueous solution was partially referred since Mg was still the dominant component in the present Mg–Ca alloy system, which included the following chemical reactions.

$$Mg(s) \rightarrow Mg^{2+}(aq) + 2e^{-}(\text{anodic reaction}) \quad (1)$$

$$2H_2O + 2e^{-} \rightarrow H_2(g) + 2OH^{-}(aq)(\text{cathodic reaction}) \quad (2)$$

$$Mg^{2+}(aq) + 2OH^{-}(aq) \rightarrow Mg(OH)_2(s)(\text{product formation}) \quad (3)$$

(1) When the fresh Mg–Ca alloy surface was exposed to the aqueous solution, the internal second phase (Mg_2Ca) acted as an efficient cathode for hydrogen evolution (Fig. 20a) because the potential of Mg_2Ca precipitate was more positive than that of the α(Mg) matrix [35]. The anodic dissolution of magnesium occurred (Eq. (1)), and the magnesium hydroxide film was expected to form on the surface of Mg–Ca alloy according to Eq. (3) due to the significant alkalization [36] near the surface (Eq. (2)). Since an increase in Mg_2Ca amount would lead to an increase in cathode-to-anode area, it could explain why in Fig. 9 the corrosion rate obtained from electrochemical tests increased with increasing Ca content.

(2) The surface film of Mg–Ca alloy was partially protective due to small micro-pores as seen in the enlarged SEM image in Fig. 4b, which was also observed on the surface film on pure Mg [37]. This porous film acted as a membrane, which was permeable to solution ingress and egress of soluble magnesium species (Fig. 20b). The surrounding solution could continuously penetrate through this kind of porous surface film and react with the inner fresh Mg–Ca alloy substrate, which led to the shift of the chemical reaction interphase inward [37]. Meanwhile, the dissolved Mg^{2+} from the Mg–Ca alloy substrate also diffused outwards through the porous $Mg(OH)_2$ film and formed $Mg(OH)_2$ at the outer surface.

(3) The growth of $Mg(OH)_2$ layer was reported to be manipulated by a dissolution–precipitation mechanism [37]. The existence of chloride would destroy the homeostasis of this dissolution–precipitation process since there was one hydration sheath, composed of a row of water molecules, in contact with the surface of Mg alloy, and Cl^{-} was small enough to displace water molecules in the hydrogen sheath [38]. Therefore, Cl^{-} preferentially combined with Mg^{2+} to transform $Mg(OH)_2$ into soluble $MgCl_2$. For the Mg–*x*Ca alloy, some pieces of $Mg(OH)_2$ protective film dissolved immediately (Fig. 20c) and made the deep fresh Mg–*x*Ca alloy substrate to expose to the solution. Then the chemical reactions (1)–(3) would cycle until the Mg–*x*Ca alloy was completely exhausted.

(4) As the biocorrosion proceeded, hydroxyapatite would be formed (Fig. 20d). The undissolved $Mg(OH)_2$ film on the surface of Mg alloy was considered to provide favorable sites for hydroxyapatite nucleation [39]. With increasing pH value, the hydroxyapatite nucleation was accelerated by increasing the supersaturation of the solution with respect to hydroxyapatite [40]. Consequently, lots of hydroxyapatite nuclei were formed on the surface film and then hydroxyapatite would grow spontaneously

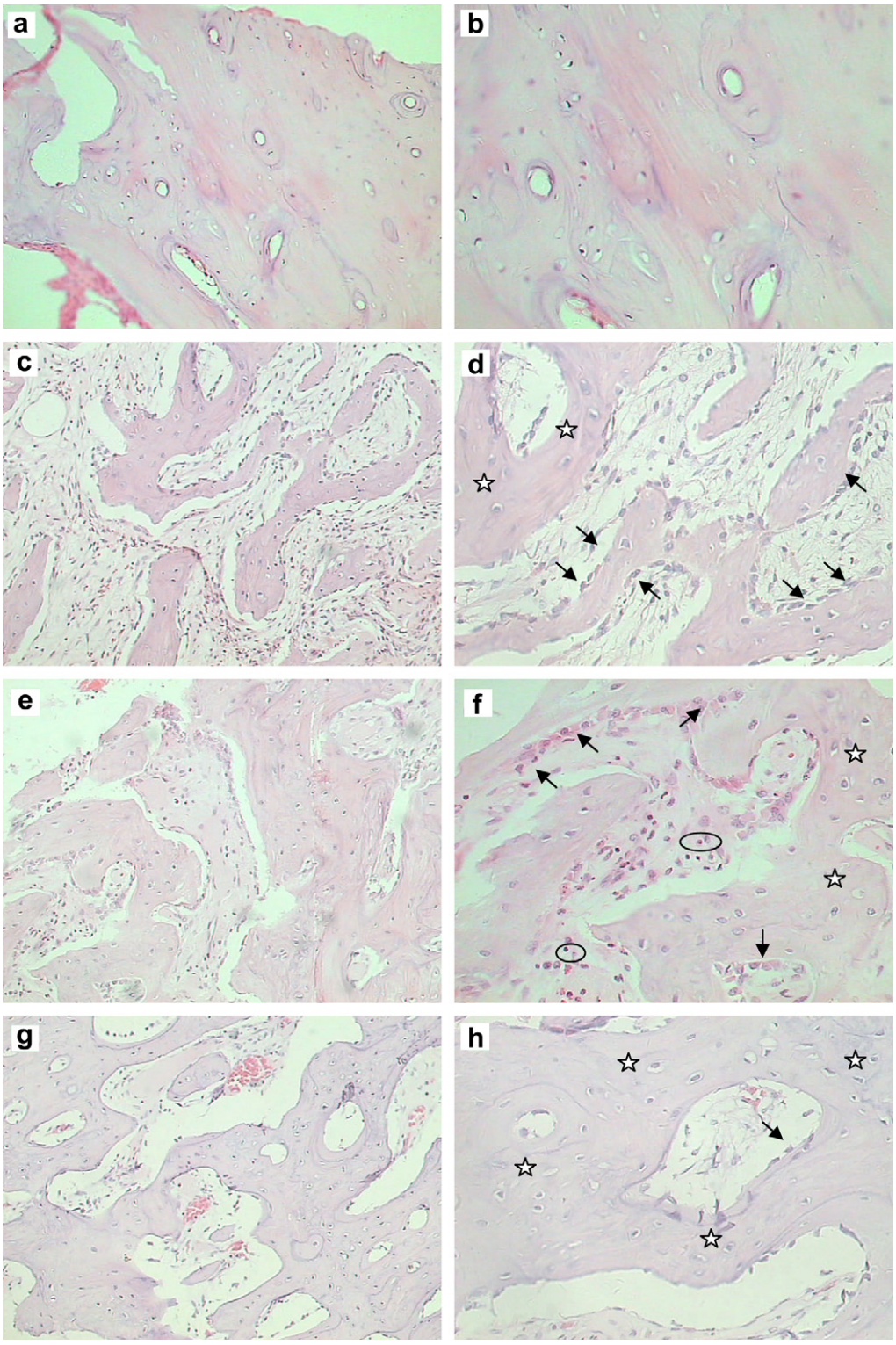

Fig. 15. Histological photographs of hematoxylin and eosin stained sections of the tissues (arrow-osteoblast; asterisk-osteocyte; circle-lymphocyte) around (a and b) c.p. Ti pins 1 month postoperation; (c and d) Mg–1Ca alloy pins 1 month postoperation; (e and f) Mg–1Ca alloy pins 2 months postoperation; (g and h) Mg–1Ca alloy pins 3 months postoperation (the magnification for (a), (c), (e) and (g) are 20× and the magnification for (b), (d), (f) and (h) are 40×).

by consuming the calcium and phosphate ions from the surrounding fluid [39].

(5) Meanwhile, the etched Mg–Ca alloy bulk would not keep integrating, sooner or later many irregular particle-shaped residues would be disintegrated from the bulk material and fall out into the surrounding medium, and the residues would be further corroded until the Mg–Ca alloy phase were exhausted (Fig. 20e). Severe non-uniform attack on

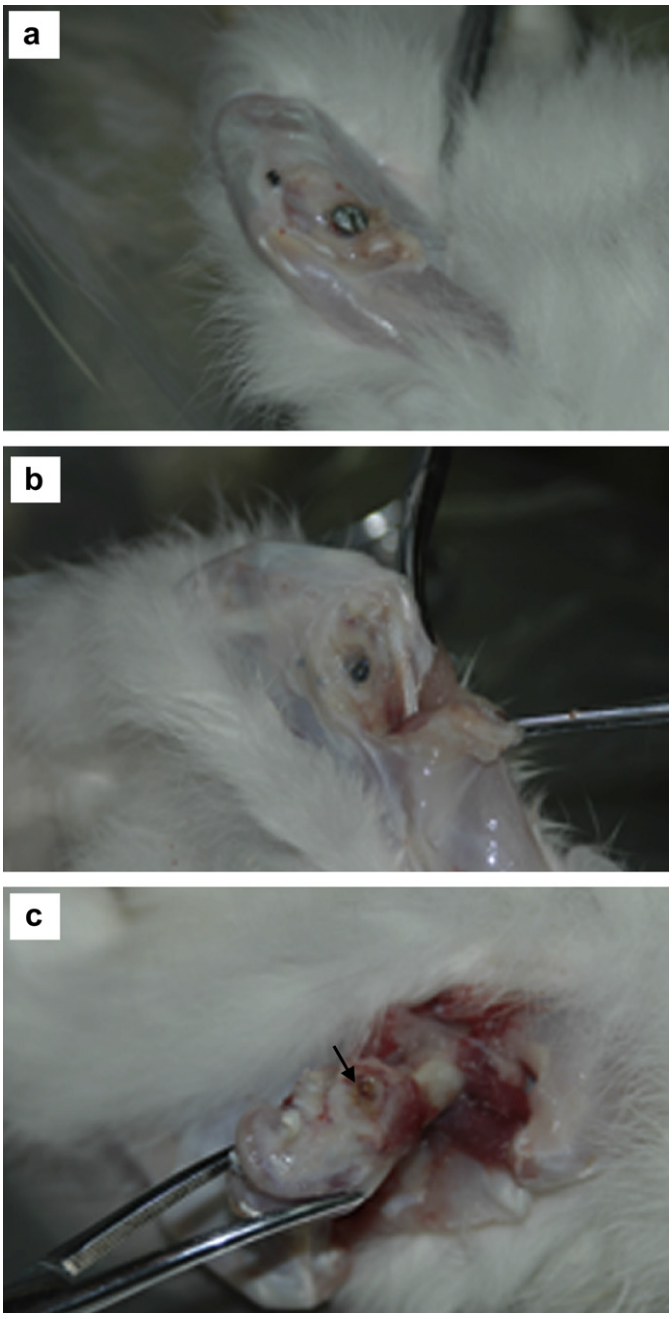

Fig. 16. The macroscopic observation of the femora with Mg–1Ca alloy pins (a) 1, (b) 2, (c) 3 months postimplantation (arrow-irregular shape hole in femora).

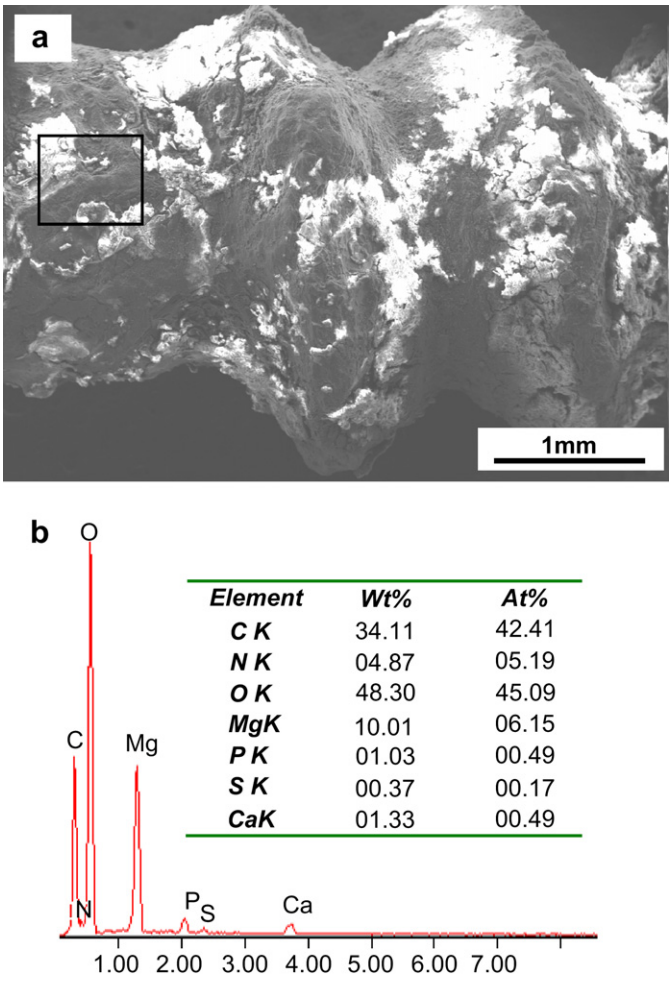

Fig. 17. (a) SEM image of the screw thread part of the retrieved Mg–1Ca alloy pin after 1 month implantation; (b) EDS spectra corresponding to the rectangular area in (a).

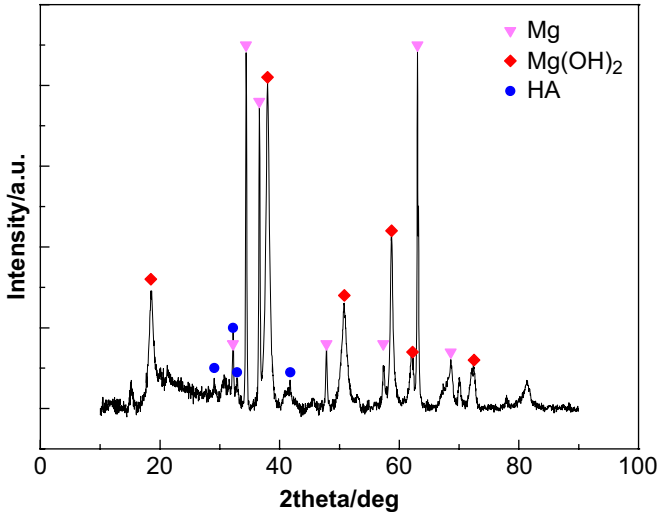

Fig. 18. X-ray diffraction patterns of the precipitates on the Mg–1Ca alloy pin after 2 months implantation.

the pure cast Mg sample was revealed by Makar et al. [41], with an SEM evidence showing that a residual Mg particle about 10 μm in diameter was locally formed by the dissolution of the surrounding matrix after 7-day immersion in sodium borate (pH = 9.2). The disintegrated particles might be endocytosed in macrophages or giant cells, and further bio-corroded in the microenvironment inside these cells, which was similar to the absorption of disintegrated calcium phosphate particles that were found to be either intracellularly digested or transported to neighboring tissues such as lymph nodes [42,43]. Witte et al. [44] had

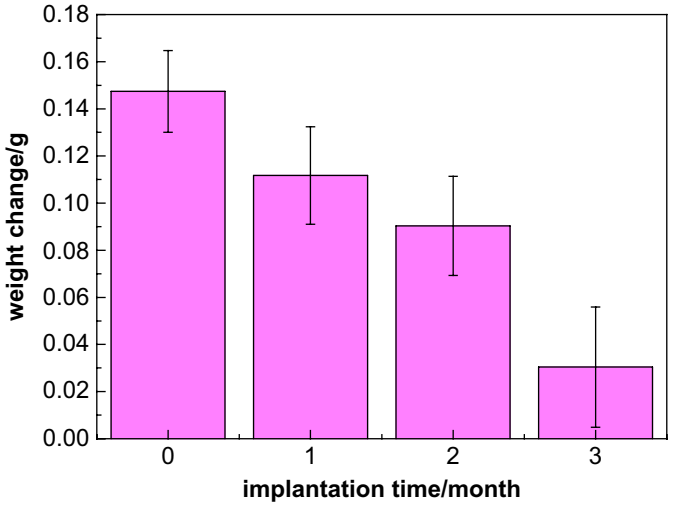

Fig. 19. The weight change of the retrieved Mg–1Ca alloy pins after 1, 2 and 3 months implantation.

revealed similar phenomenon (small corrosion products incorporated inside the giant cells) for the biodegradable AZ91D porous scaffolds.

The X-ray diffraction results (as shown in Fig. 18) of the *in vivo* biocorrosion products, showed the same phases ($Mg(OH)_2$ and hydroxyapatite), as that of *in vitro* biocorrosion products. Therefore, it could be inferred that *in vitro* and *in vivo* biocorrosions of Mg–Ca alloy should be based on the same mechanism. Yet it could be noticed that the biocorrosion rate (2.28 ± 0.13 mg/mm^2/yr) of Mg–1Ca alloy *in vivo* was much slower than that of *in vitro* electrochemical tests (average 10.49 mg/mm^2/yr). The following factors might be responsible for the retardment of corrosion rate.

(1) One factor was the lower concentration of chloride ions present in blood plasma (103 mM) [19] and bone (48.6–56.7 mM) [1,45] compared to that in SBF (147.8 mM). The low mass loss in DMEM of AZ91D-HA composites in artificial seawater was analogously attributed to low chloride concentration [46].

(2) Proteins, which affected metallic corrosion usually by changing either anodic or cathodic process, or both [47–49], might be another factor to influence *in vivo* biocorrosion of Mg–1Ca alloy. Liu et al. [50] found that the addition of bovine serum albumin moved the open-circuit potential of AZ91 toward a more positive value and suppressed the corrosion reaction. Muller et al. [51] also reported that the potential range of the passivation region was extended in the presence of albumin for LAE442 and AZ31 magnesium alloys.

Compared to the biocorrosion rate of AZ31, AZ91D, WE43, and LAE442 reported by Witte et al. [4,5], the biocorrosion rate of the present as-cast Mg–1Ca alloy was faster (Table 2). To meet the requirement of the synchronization between the implant biodegradation and the new bone formation, several strategies might be feasible to regulate the biocorrosion rate of Mg–Ca alloys.

(1) *The addition of other elements*. As reported by Song [52], besides Ca, the elements which could be tolerated in the human body and could also retard the biocorrosion of magnesium alloys were Zn, Mn, and perhaps a very small amount of rare earth elements with low toxicity. The rare earth elements were found to increase the resistance to the Mg^{2+} cation egress through MgO layer in Mg–RE alloy [53]. Mn was previously added to many commercial alloys to improve corrosion resistance by reducing the harmful effect of impurities [2].
(2) *Hot working and/or heat treatment*. Liu et al. [54] had reported that a solid solution or ageing treatment could effectively change the distribution and amount of $Mg_{17}Al_{12}$ phase and improve the corrosion resistance. Denkena and Lucas. [55] had found that the degradation kinetics of magnesium alloys was determined by the manufacturing process.
(3) *Surface modification*. Most of the physical and chemical surface modification techniques should be effective to prolong the degradation time. For example, anodizing treatments on Mg alloy could deposit a hard ceramic-like coating that offers both abrasion resistance and corrosion

Table 2
Mechanical properties and corrosion rate of Mg alloys reported as potential orthopedic implants

Alloy/working history	UTS (MPa)	Elongation (%)	V_{corr}/*in vitro* (mm/yr)	V_{corr}/*in vivo*[a] (mg/mm^2/yr)	References
AZ31/gravity-cast	260	15	–	1.17	[4,25]
AZ91D/gravity-cast	230	3	2.8	1.38	[5,26]
WE43/gravity-cast	220	2	–	1.56	[4,26]
LAE442/gravity-cast	–	–	6.9	0.39	[5]
MMC-HA/as-extruded	325	3.5	1.25	–	[27]
Mg–2Ca/rapidly solidified	380	7.3	–	–	[28]
Mg–1Ca/as-extruded	239.63	10.63	1.74	–	Present study
Mg–1Ca/as-rolled	166.7	3	1.63	–	Present study
Mg–1Ca/as-cast	71.38	1.87	12.56	2.28	Present study

[a] The corrosion rate could be expressed by the weight loss of alloys/yr, $V_{corr} = \rho \Delta V/St$, in which ρ was the standard density of alloy, ΔV was the reduction of implant volume, S was the initial implant surface exposed to corrosion medium, and t was the exposure time. The *in vivo* corrosion rate of AZ31, AZ91D, WE43, and LAE442 were deduced from the literatures [4] (3.2 mm^2/yr for AZ31, 4.13 mm^2/yr for WE43) and [5] (74.51 mm^3/yr for AZ91D, 23.68 mm^3/yr for LAE442).

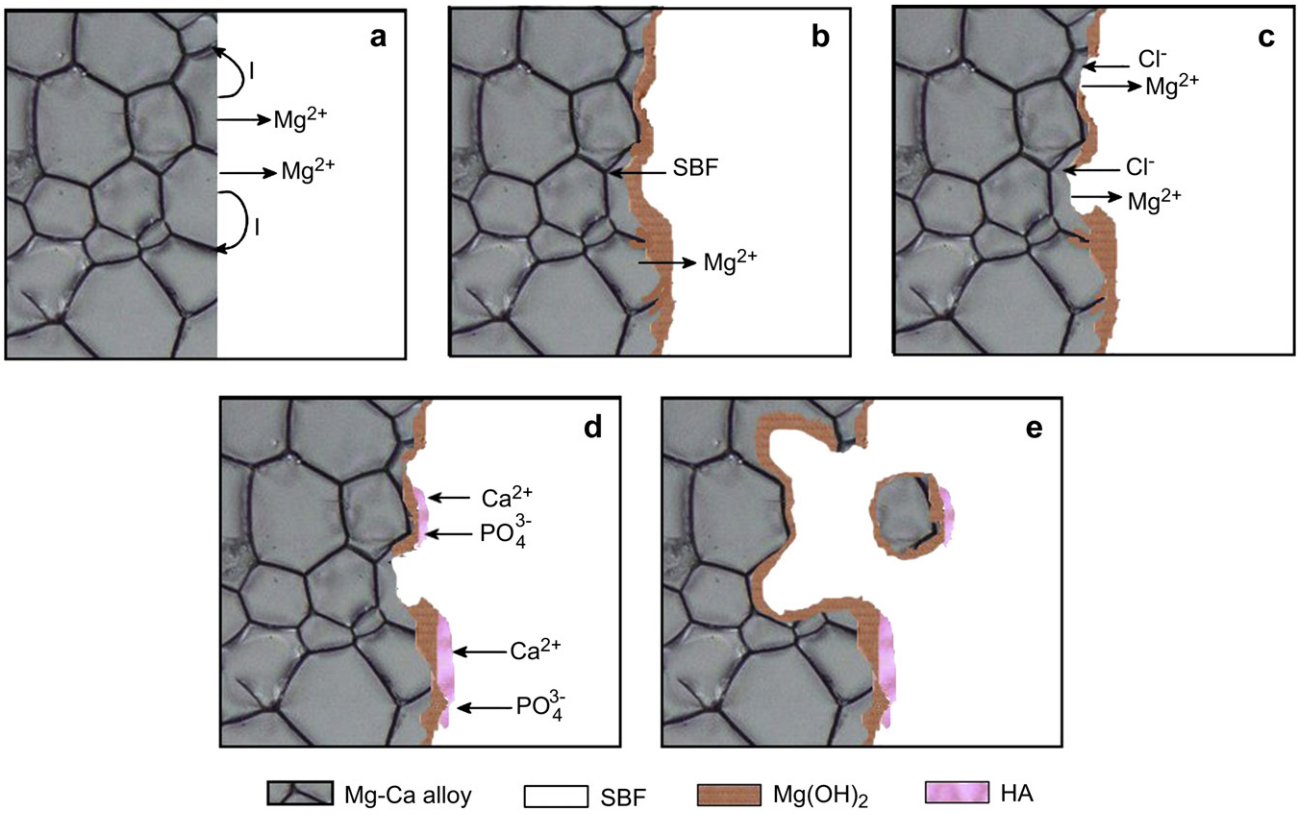

Fig. 20. Schematic diagram of the alloy/solution biocorrosion interface: (a) the galvanic corrosion between Mg and Mg_2Ca phase, (b) the partially protective film covering the surface of Mg–Ca alloys, (c) the adsorption of chloride ions to transform $Mg(OH)_2$ into $MgCl_2$, (d) the hydroxyapatite formation by consuming Ca^{2+} and PO_4^{3-}, and (e) the disintegrated particle-shape residues falling out of the bulk substrate.

protection [52]. To guarantee the complete biodegradation of the resulting composite, coating the surface of Mg alloy with a layer of degradable polyester or calcium phosphate will be a good choice.

5. Conclusions

In the present study, we developed binary Mg–Ca alloys for use as biodegradable materials within bone. The Mg–Ca alloys were mainly composed of two phases α(Mg) and Mg_2Ca, and their mechanical properties and biocorrosion behaviors could be adjusted by controlling the Ca content and the processing treatment. A mixture of $Mg(OH)_2$ and hydroxyapatite precipitated on the surface of Mg–1Ca alloy with the extension of immersion and implantation time. The cytocompatibility evaluation using L-929 cells revealed that Mg–1Ca alloy did not induce toxicity to cells. High activity of osteoblast and osteocytes were observed around the Mg–1Ca alloy pin, implanted into the rabbit femoral shafts, respectively, for 1, 2 and 3 months. Radiographic examination revealed that the Mg–1Ca alloy pins gradually degraded *in vivo* within 90 days and newly formed bone was clearly seen at month 3. In addition, no significant difference ($p > 0.05$) of serum magnesium was detected at different degradation stages. All these biocompatibility tests of Mg–1Ca alloy demonstrated its qualification as orthopedic biodegradable materials.

Acknowledgement

This work was supported by the National Natural Science Foundation of China (No. 30670560) The authors would like to thank Mr. C. Li (now a PhD student at Curtin University of Technology, Australia) and Dr. Y. Cheng (now a senior engineer at Beijing Institute of Non-ferrous Metals, China), who previously studied at Peking University, China, for the assistance in the early experiments, and thank Prof. L.J. Chen at Shenyang University of Technology, China, for the hot extrusion process work on the experimental alloys.

References

[1] Staigera MP, Pietaka AM, Huadmaia J, Dias G. Magnesium and its alloys as orthopedic biomaterials: a review. Biomaterials 2006;27:1728–34.
[2] Song GL, Andrej A. Corrosion mechanisms of magnesium alloys. Adv Eng Mater 1999;1:11–33.
[3] Li L, Gao J, Wang Y. Evaluation of cyto-toxicity and corrosion behavior of alkali–heat-treated magnesium in simulated body fluid. Surf Coat Technol 2004;185:92–8.
[4] Witte F, Kaese V, Switzer H, Meyer-Lindenberg A, Wirth CJ, Windhag H. In vivo corrosion of four magnesium alloys and the associated bone response. Biomaterials 2005;26:3557–63.
[5] Witte F, Fischer J, Nellesen J, Crostack H, Kaese V, Pischd A, et al. In vitro and in vivo corrosion measurements of magnesium alloys. Biomaterials 2006;27:1013–8.

[6] Heublein B, Rohde R, Kaese V, Niemeyer M, Hartung W, Haverich A. Biocorrosion of magnesium alloys: a new principle in cardiovascular implant technology? Heart 2003;89:651–6.
[7] Zartner P, Cesnjevar R, Singer H, Weyand M. First successful implantation of a biodegradable metal stent into the left pulmonary artery of a preterm baby. Catheter Cardiovasc Interv 2005;66:590–4.
[8] Schranz D, Zartner P, Michel-Behnke I, Akinturk H. Bioabsorbable metal stents for percutaneous treatment of critical recoarctation of the aorta in a newborn. Catheter Cardiovasc Interv 2006;67:671–3.
[9] Kuwahara H, Al-Abdullat Y, Mazaki N, Tsutsumi S, Aizawa T. Precipitation of magnesium apatite on pure magnesium surface during immersing in Hank's solution. Mater Trans 2001;42:1317–21.
[10] Mani G, Feldman Marc D, Patel D, Agrawal M. Coronary stents: a materials perspective. Biomaterials 2007;28:1689–710.
[11] El-Rahman SSA. Neuropathology of aluminum toxicity in rats (glutamate and GABA impairment). Pharmacol Res 2003;47:189–94.
[12] Yumiko N, Yukari T, Yasuhide T, Tadashi S, Yoshio I. Differences in behavior among the chlorides of seven rare earth elements administered intravenously to rats. Fundam Appl Toxicol 1997;37:106–16.
[13] Ilich JZ, Kerstetter JE. Nutrition in bone health revisited: a story beyond calcium. J Am Coll Nutr 2000;19:715–37.
[14] Serre CM, Papillard M, Chavassieux P, Voegel JC, Boivin G. Influence of magnesium substitution on a collagen–apatite biomaterial on the production of a calcifying matrix by human osteoblasts. J Biomed Mater Res 1998;42:626–33.
[15] Alloy phase diagram. In: ASM handbook, vol. 3. ASM International, The Materials Information Company; 1992.
[16] Lloyd AW. Interfacial bioengineering to enhance surface biocompatibility. Med Device Technol 2002;13:18–21.
[17] John CM, Arthur JT. Synthetic biodegradable polymers as orthopedic devices. Biomaterials 2000;21:2335–46.
[18] ASTM-E8-04: standard test methods for tension testing of metallic materials, Annual book of ASTM standards. Philadelphia, PA, USA: American Society for Testing and Materials; 2004.
[19] Kokubo T, Takadama H. How useful is SBF in predicting in vivo bone bioactivity? Biomaterials 2006;27:2907–15.
[20] ASTM-G31-72: standard practice for laboratory immersion corrosion testing of metals, Annual book of ASTM standards. Philadelphia, PA, USA: American Society for Testing and Materials; 2004.
[21] ISO-10993–5: biological evaluation of medical devices – part 5: tests for cytotoxicity: in vitro methods, ANSI/AAMI, Arlington, VA; 1999.
[22] Genevieve B, Nadine P. The corrosion of pure magnesium in aerated and deaerated sodium sulphate solutions. Corr Sci 2001;43:471–84.
[23] Jian-Wei C, Xing-Wu G, Peng-Huai F, Li-Ming P, Wen-Jiang D. Effect of heat treatment on corrosion and electrochemical behavior of Mg–3Nd–0.2Zn–0.4Zr (wt%) alloy. Electrochim Acta 2007;52:3160–7.
[24] ASTM-G102-89: standard practice for calculation for corrosion rates and related information from electrochemical measurements, Annual book of ASTM standards. Philadelphia, PA, USA: American Society for Testing and Materials; 1999.
[25] www.magnesium-electron.com.
[26] Avedesian MM, Baker H. Magnesium and magnesium alloys, ASM specialty handbook. ASM International, The Materials Information Society; 1999.
[27] Shikinami Y, Okuno M. Bioresorbable devices made of forged composites of hydroxyapatite (HA) particles and poly-L-lactide (PLLA): part I. Basic characteristics. Biomaterials 1999;20:859–77.
[28] Takeshi M, Junichi K, Makomoto S. Structures and properties of rapidly solidified Mg–Ca based alloys. Mater Sci Eng 1994;A181/A182:1410–4.
[29] Zreiqat H, Howlett CR, Zannettino A, Evans P, Schulze-Tanzil G, Knabe C, et al. Mechanisms of magnesium-stimulated adhesion of osteoblastic cells to commonly used orthopaedic implants. J Biomed Mater Res 2002;A62:175–84.
[30] Kaouther A, Takashi S, Wolfgang HG, Dahmani MF, Xiong JP, Arnaout MA. Binding affinity of metal ions to the CD11b A-domain is regulated by integrin activation and ligands. J Biol Chem 2004; 279:25483–8.
[31] Jin-Woo P, Kwang-Bum P, Jo-Young S. Effects of calcium ion incorporation on bone healing of Ti6Al4V alloy implants in rabbit tibiae. Biomaterials 2007;28:3306–13.
[32] Nayab SN, Jones FH, Olsen I. Effects of calcium ion implantation on human bone cell interaction with titanium. Biomaterials 2005;26:4717–27.
[33] Vormann J. Magnesium: nutrition and metabolism. Mol Aspects Med 2003;24:27–37.
[34] Sojka JE, Weaver CM. Magnesium supplementation and osteoporosis. Nutr Rev 1995;53:71–80.
[35] Kim JG, Kim YW. Advanced Mg–Mn–Ca sacrificial anode materials for cathodic protection. Mater Corros 2001;52:137–9.
[36] Song GL, Atrens A, St. John D, Nairn J, Li Y. The electrochemical corrosion of pure magnesium in 1 N NaCl. Corr Sci 1997;39:855–75.
[37] Nordlien JH, Ono S, Masuko N, Nisancioclu K. A TEM investigation of naturally formed oxide films on pure magnesium. Corr Sci 1997;39: 1397–414.
[38] Talbot DEJ, Talbot JDR. Corrosion science and technology. CRC Press; 1998.
[39] Kokubo T. Formation of biologically active bone-like apatite on metals and polymers by a biomimetic process. Thermochimica Acta 1996;280/281:479–90.
[40] Jonasova L, Muller FA, Helebrant A, Strnad J, Greil P. Biomimetic apatite formation on chemically treated titanium. Biomaterials 2004;25:1187–94.
[41] Makar GL, Kruger J. Corrosion studies of rapidly solidified magnesium alloys. J Electrochem Soc 1990;137:414–21.
[42] Klein CP, de Groot K, Driessen AA, Ven der Lubbe HBM. Interaction of biodegradable β-whitlockite ceramics with bone tissue: an in vivo study. Biomaterials 1985;6:189–92.
[43] Lu JX, Descamps M, Dejou J, Koubi G, Hardouin P, Lemaitre J, et al. The biodegradation mechanism of calcium phosphate biomaterials in bone. J Biomed Mater Res 2002;63:408–12.
[44] Witte F, Ulrich H, Rudert M, Willbold E. Biodegradable magnesium scaffolds: part I: appropriate inflammatory response. J Biomed Mater Res 2007;A81:748–56.
[45] William RA, Thomas PN, Arthur GM, Dorothy B. The relationship between tissue chloride and plasma chloride. Am J Physiol 1937;22: 224–35.
[46] Witte F, Feyerabend F, Maier P, Fischer J, Stormer M, Blawert C, et al. Biodegradable magnesium–hydroxyapatite metal matrix composites. Biomaterials 2007;28:2163–74.
[47] Zhu JJ, Xu NX, Zhang CD. Characteristics of copper corrosion in simulated uterine fluid in the presence of protein. Adv Contracept 1999;15:179–90.
[48] Khan MA, Williams RL, Williams DF. The corrosion behavior of Ti–6Al–4V, Ti–6Al–7Nb and Ti–13Nb–13Zr in protein solutions. Biomaterials 1999;20:631–7.
[49] Cheng XL, Roscoe SG. Corrosion behavior of titanium in the presence of calcium phosphate and serum proteins. Biomaterials 2005;26:7350–6.
[50] Liu CL, Xin YC, Tian XB, Chu PK. Degradation susceptibility of surgical magnesium alloy in artificial biological fluid containing albumin. J Mater Res 2007;22:1806–14.
[51] Muller WD, Nascimento ML, Zeddies M, Corsico M, Gassa LM, Lorenzo de Mele MAF. Magnesium and its alloys as degradable biomaterials corrosion studies using potentiodynamic and EIS electrochemical techniques. Mater Res 2007;10:5–10.
[52] Song GL. Control of biodegradation of biocompatible magnesium alloys. Corr Sci 2007;49:1696–701.
[53] Zucchi F, Grassi V, Frignani A, Monticelli C, Trabanelli G. Electrochemical behavior of a magnesium alloy containing rare earth elements. J Appl Electrochem 2006;36:195–204.
[54] Liu CL, Xin YC, Tang GY, Chu PK. Influence of heat treatment on degradation behavior of bio-degradable die–cast AZ63 magnesium alloy in simulated body fluid. Mater Sci Eng A 2007;456:350–7.
[55] Denkena B, Lucas A. Biocompatible magnesium alloys as absorbable implant materials—adjusted surface and subsurface properties by machining processes. Manuf Technol 2007;56:113–6.